JGR Solid Earth

RESEARCH ARTICLE
10.1029/2022JB025555

Key Points:

- Combined seismic and geodetic (seismogeodetic) data enable rapid earthquake magnitude estimates
- Seismogeodetic magnitude estimates for very large earthquakes are timelier than those based on seismic data alone
- The seismogeodetic method is applicable to earthquakes with complex source mechanisms, including tsunami earthquakes

Supporting Information:

Supporting Information may be found in the online version of this article.

Correspondence to:

D. Golriz,
dgolriz@ucsd.edu

Citation:

Golriz, D., Hirshorn, B., Bock, Y., Weinstein, S., & Weiss, J. R. (2023). Real-time seismogeodetic earthquake magnitude estimates for local tsunami warnings. *Journal of Geophysical Research: Solid Earth*, *128*, e2022JB025555. https://doi.org/10.1029/2022JB025555

Received 5 SEP 2022
Accepted 21 DEC 2022
Corrected 7 FEB 2023

This article was corrected on 7 FEB 2023. See the end of the full text for details.

Author Contributions:

Conceptualization: Dorian Golriz, Barry Hirshorn, Yehuda Bock
Data curation: Dorian Golriz, Yehuda Bock
Formal analysis: Dorian Golriz, Barry Hirshorn
Funding acquisition: Yehuda Bock
Investigation: Dorian Golriz, Barry Hirshorn
Methodology: Dorian Golriz, Barry Hirshorn
Project Administration: Yehuda Bock, Stuart Weinstein
Resources: Dorian Golriz, Barry Hirshorn, Jonathan R. Weiss
Software: Dorian Golriz

Real-Time Seismogeodetic Earthquake Magnitude Estimates for Local Tsunami Warnings

Dorian Golriz[1], Barry Hirshorn, Yehuda Bock[1], Stuart Weinstein[2], and Jonathan R. Weiss[2]

[1]Institute of Geophysics and Planetary Physics, Scripps Institution of Oceanography, University of California San Diego, La Jolla, CA, USA, [2]Pacific Tsunami Warning Center, National Oceanic and Atmospheric Administration, National Weather Service, Ewa Beach, HI, USA

Abstract We estimate a seismogeodetic earthquake moment magnitude using unclipped, broadband velocity and displacement waveforms from collocated Global Navigation Satellite Systems and seismic stations located within 800 km epicentral distance for nine $7.2 < M_w < 9.1$ earthquakes. We consider the vertical component of seismogeodetic displacement as an approximate source time function and integrate the associated time series to obtain the seismic moment. By continuing to integrate vertical displacement beyond the initial *P*-waves, we obtain rapid estimates of M_w that are within 0.2 magnitude units for 8 thrust faulting events and within 0.3 units for the single normal faulting event. Because our estimates of the seismic moment are based on the maximum value of integrated displacement, no regression against other source parameters, or distance, is necessary. Our new method shows promise for integration into earthquake and local tsunami early warning systems, including tsunami earthquakes characterized by relatively slow moment release over a longer rupture time, and earthquakes with complex source time functions.

Plain Language Summary Tsunami Warning Centers are responsible for alerting coastal populations of expected tsunami waves caused by significant earthquakes. Traditionally, warnings rely on rapid magnitude estimation based on distant seismic data. This is sufficient for ocean-wide tsunami warnings but often not for coastal populations closest to a causative earthquake. More timely warnings for local tsunamis can be obtained by supplementing measurements of seismic accelerations with displacements from Global Navigation Satellite Systems instruments located close to the earthquake source. In this study, we use this data combination to estimate the magnitude of nine historical earthquakes around the Pacific basin. Our real-time simulations show that we can obtain useful and reliable magnitude estimates for large earthquakes and issue local tsunami warnings within minutes after rupture initiation.

1. Introduction

Tsunamis are a devastating natural, high-fatality hazard (Bryant, 2008). Because most tsunamis are generated by earthquakes, the first indication of a potentially life-threatening tsunami is the earthquake itself. Effective tsunami warning systems must therefore detect, locate, and estimate the magnitude of the causative earthquake to infer tsunamigenic potential, and warn coastal populations as soon as possible after initiation of fault rupture. Rapid characterization of the earthquake focal mechanism also aids in inferring tsunamigenic potential (Melgar & Bock, 2015; Melgar et al., 2016). Most tsunamis originate from Earth's subduction zones due to thrust faulting although earthquakes with other source mechanisms have also generated tsunamis (Elbanna et al., 2021; Scott, 2021). For example, the 2012 M_w8.6 predominantly strike-slip intraplate event off Sumatra, Indonesia (Satriano et al., 2012), generated a tsunami that was recorded at sea-level stations as far as 4,800 km from the epicenter and by ocean bottom pressure sensors (i.e., DART buoys) in the Indian Ocean (Wang et al., 2012). Similarly, the 2009 M_w8.1 Samoa earthquake was a normal faulting, outer-rise type event that produced a sizable tsunami with 189 fatalities (Okal et al., 2010).

Current warning systems are well-developed for basin-wide and regional tsunamis. For earthquakes over M_w8.0, they rely mainly on long period (>∼300 s) seismic data recorded by broadband seismometers at distances greater than ∼500 km from the epicenter. However, for large tsunamigenic events, ground motions can exceed the dynamic range of a seismometer and result in a clipped record if measured too close to the seismic rupture. Therefore, tsunami warnings to the coastal communities located closest to the earthquake rupture may not be issued in a sufficiently timely manner. Another serious challenge for tsunami warning is the identification of tsunami

Supervision: Yehuda Bock, Stuart Weinstein
Validation: Dorian Golriz
Visualization: Dorian Golriz, Jonathan R. Weiss
Writing – original draft: Dorian Golriz, Barry Hirshorn, Yehuda Bock, Stuart Weinstein, Jonathan R. Weiss
Writing – review & editing: Yehuda Bock, Stuart Weinstein

earthquakes that release very little high-frequency energy that can be felt by humans (Kanamori, 1972; Polet & Kanamori, 2000; Tanioka et al., 1997). In this case, the predicted amplitudes of the tsunami waves generated may be underestimated.

A prototypical example of the over-reliance on seismic data is the 2011 M_w9.1 Tohoku-Oki, Japan earthquake and tsunami that devastated the northeast coast of Honshu. The Japan Meteorological Agency (JMA) determined a magnitude M_w7.9 and issued a tsunami warning within 3 min of rupture initiation. This underestimate may have resulted in a delay of coastal evacuation (Hoshiba & Ozaki, 2014). Improved seismic methods have been developed to increase timeliness and accuracy, in particular the inversion of the W-phase (Kanamori, 1993) to obtain the W-phase Centroid Moment Tensor (WCMT) (Kanamori & Rivera, 2008) and corresponding moment magnitude, M_w. The WCMT and M_w can be available within 5–20 min of earthquake origin time, thus making it more suitable for local tsunami warning (Rivera & Kanamori, 2009). Another issue with insufficiently broadband seismic data is magnitude saturation for earthquakes greater than $\sim M_w$8.0, which can result in significant magnitude underestimates (Kanamori, 1977), as occurred in the JMA response to the 2011 M_w9.1 Tohoku-Oki event (Hoshiba & Ozaki, 2014).

Seismic networks also include strong-motion accelerometers that do not clip. However, for earthquake source parameter determination methods requiring surface displacement information, acceleration waveforms must be doubly integrated, often causing drifts in displacement as a result of baseline errors (Boore, 2001; Boore et al., 2002; Graizer, 1979; Iwan et al., 1985; Melgar, Bock, et al., 2013; Smyth & Wu, 2007). To improve local tsunami warnings, other real-time sensors may be deployed. For example, ocean-bottom pressure sensors, near-shore Global Navigation Satellite Systems (GNSS)-mounted buoys, autonomous wave gliders, and seafloor GNSS-acoustic instruments (Hoshiba & Ozaki, 2014; Kido et al., 2011; Sato et al., 2013; Yokota et al., 2018). Furthermore, real-time GNSS networks can measure precise (∼1 cm single epoch) high-rate (1–10 Hz) displacements including dynamic and static (permanent) coseismic offsets, while not experiencing clipping or magnitude saturation (e.g., Bock et al., 2000, 2004; Genrich & Bock, 2006; Larson et al., 2003; Wright et al., 2012).

Empirical scaling relationships using peak-ground-displacements (PGDs) measured from high-rate GNSS displacements (Crowell et al., 2013; Melgar et al., 2015; Ruhl et al., 2019) have been successfully used to rapidly estimate magnitude in earthquake early warning contexts (Hodgkinson et al., 2020; Mattioli et al., 2020; Melbourne et al., 2021). Retrospective studies of several tsunamigenic events in Japan and Chile have also demonstrated the utility of scaling relationships as an element of tsunami warning systems and to derive models of coastal inundation (Blewitt et al., 2006; Melgar et al., 2016; Ohta et al., 2012). Several earthquake early warning systems have already incorporated GNSS displacement data into their magnitude determination algorithms. These include GlarmS (Grapenthin et al., 2014) and BEFORES (Minson et al., 2014) in the Western U.S., G-FAST in the Western U.S. and Chile (Barrientos, 2018; Crowell et al., 2018), and REGARD in Japan (Kawamoto et al., 2016). In addition to rapid magnitude estimation, studies have demonstrated that GNSS displacements can provide rapid centroid moment tensor solutions (Käufl et al., 2014; Melgar et al., 2012; O'Toole et al., 2013) and finite fault slip models (e.g., Langbein et al., 2005; Melgar, Crowell, et al., 2013; Miyazaki et al., 2004).

GNSS displacements, however, are not as precise as integrated seismic velocities or double-integrated accelerations and cannot detect *P*-waves. Thus, GNSS networks require a seismic trigger for detection and hypocenter location. Combining GNSS and collocated strong-motion data (Bock et al., 2011; Emore et al., 2007; Nikolaidis et al., 2001; Smyth & Wu, 2007) yields unclipped broadband velocity and displacement waveforms that are sensitive to the entire spectrum of ground motions from the Nyquist frequency of the accelerometer data (typically 50–100 Hz) to the static coseismic offset, while minimizing baseline errors.

Here we use seismogeodetic networks consisting of collocated GNSS receivers and strong-motion accelerometers to improve local tsunami warnings through rapid estimation of earthquake magnitude. The separation distance between GNSS and strong motion instruments can be as much as 15 km as long as the time offset between sensors in considered (Emore et al., 2007). However, we set a maximum separation distance of 5 km (Bock et al., 2011; Saunders et al., 2016), and more than 90% of the sensors in this study are within 4 km. Ideally, to optimize the combination of the two data types, the instruments should be collocated (also for logistical simplicity). For example, an inexpensive Micro-Electro Mechanical System accelerometer directly attached to the GNSS monument has been deployed at multiple stations in California; the system has been successfully demonstrated in the near field of several M_w4+ earthquakes (Goldberg & Bock, 2017; Saunders et al., 2016).

We designed a Kalman filter to optimally combine the GNSS displacements and strong motion accelerations (Bock et al., 2011; Smyth & Wu, 2007) to estimate seismogeodetic velocities and displacements. The seismogeodetic velocities are used to detect *P*-wave onset times and estimate the coseismic time window (Golriz et al., 2021) over a network of near- to far-field collocated GNSS and accelerometer stations. Using the vertical component of seismogeodetic displacement as an approximate source time function (Kikuchi & Ishida, 1993; Tsuboi et al., 1995), we rapidly estimate the seismic moment and M_w. Our method is based on theory (Aki & Richards, 2002), unlike empirical magnitude scaling relationships such as PGD. Using the seismogeodetic data from nine earthquakes in the $7.2 < M_w < 9.1$ range, we estimate the seismogeodetic moment magnitude, M_{wg}, within 2–3 min of earthquake origin time with an accuracy of 0.18 magnitude units for eight thrust faulting events and 0.32 magnitude units for a single normal faulting event.

1.1. Operational Tsunami Warning at the Pacific Tsunami Warning Center

This study is motivated by our goal of developing an operational seismogeodetic-based warning system for local tsunamis (Figure S1 in Supporting Information S1). Although applicable to any tsunami warning center, we use our work with the National Oceanic and Atmospheric Administration/National Weather Service/Pacific Tsunami Warning Center (PTWC), to illustrate our methodology. Rapid magnitude estimation based on seismic data is one component of the current tsunami warning system at PTWC, which performs real-time data reception, earthquake detection, location, and W-phase inversion.

It is instructive to describe the current PTWC system at as an example of a real-world operation that can then be useful to other tsunami warning efforts, as well as for earthquake early warning. The PTWC system operates partially within an Earthworm environment (https://www.isti.com/ and http://www.earthwormcentral.org/). Automated earthquake picking, association, magnitude estimation, and paging (R. Allen, 1982; R. V. Allen, 1978; Evans & Allen, 1983; Johnson et al., 1995, 1997; Withers et al., 1998) notifies duty scientists of a potential tsunami within 2–5 min of the beginning of any earthquake greater than $\sim M_w 5.5$, worldwide. In the Hawaiian Islands, Puerto Rico, and the Virgin Islands, the PTWC duty scientists are paged for earthquakes greater than $\sim M_w 3.5$ within 10–20 s of earthquake origin time (Hirshorn, 2007; Hirshorn et al., 2019).

PTWC duty scientists assess the tsunamigenic potential of an earthquake using a variety of magnitude estimation techniques, based on different periods contained in the earthquake source spectrum (Hirshorn & Weinstein, 2009; Hirshorn et al., 2019), recorded in regional to teleseismic broadband data. The most accurate estimate of M_w comes from the inversion of the W-phase (Kanamori, 1993) to obtain the WCMT (Kanamori & Rivera, 2008) within ~25 min of earthquake origin time. Rivera and Kanamori (2009) showed that the W-phase is useful for regional tsunami warnings by improving the timeliness from approximately 25 to 5 min after earthquake origin time. Regional implementations are operating in Japan, Mexico, Australia, Taiwan, China, and Chile. In Chile, the W-Phase method has been running automatically in real-time for the Centro Sismológico Nacional (CSN) since 2011 for regional distances, providing a WCMT and M_w within 5–6 min of earthquake origin time (Riquelme et al., 2016, 2018). Although not yet implemented in real-time operations, PTWC is testing a regional WCMT modification, which will report M_w and the moment tensor within ~15 min. See Hirshorn and Weinstein (2009) and Hirshorn et al. (2019) for a review of PTWC source characterization methods.

The broadband *P*-wave moment magnitude, M_{wp} (Tsuboi et al., 1995, 1999; Whitmore et al., 2002) provides PTWC with initial estimate of M_w. The M_{wp} method relies on the first *P*-waves, typically providing accurate estimates of M_w within about 2–5 min of rupture initiation. However, M_{wp} estimates of M_w have three important caveats. First, for very large ($M_w > 8.0$) earthquakes, M_{wp} may saturate when based on data from seismic sensors with insufficient long period (e.g., <350 s) sensitivity. Second, for complex earthquakes with several source time function peaks that are well separated in time, M_{wp} may underestimate M_w. Third, and perhaps the most challenging for a tsunami warning system, is the identification of "tsunami" or "slow" earthquakes (Kanamori, 1972). M_{wp} may underestimate the magnitude of these events because of their relatively slow moment release over a longer rupture time. M_{wg} can potentially address these caveats, enabling PTWC to issue local tsunami warnings with accurate magnitude estimates and within 2–3 min of earthquake origin time.

PTWC issues its first tsunami threat message for any shallow (<100 km) undersea or nearshore earthquake in or near the vicinity of the Pacific basin with a magnitude greater than $M_w 7.0$. If the magnitude is in the 7.1–7.5 range, the message will indicate a possible tsunami threat to coasts located within 300 km of the epicenter. If

Table 1
Earthquakes Used in This Study

Name/Region	M_w[a]	Fault mechanism	Origin time (UTC)[b]	Longitude (E°)	Latitude (N°)	Depth (km)
Tokachi-Oki, Japan	8.3	Reverse	25 September 2003 19:50:07	144.079	41.780	42.0
Maule, Chile	8.8	Reverse	27 February 2010 06:34:11	−72.898	−36.122	22.9
Tohoku-Oki, Japan	9.1	Reverse	11 March 2011 05:46:24	142.861	38.104	23.7
Iquique, Chile	8.1	Reverse	01 April 2014 23:46:47	−70.769	−19.610	25.0
Illapel, Chile	8.3	Reverse	16 September 2015 22:54:32	−71.674	−31.573	22.4
Chiapas, Mexico	8.2	Normal	08 September 2017 04:49:19	−93.899	15.022	47.4
Kilauea, Hawaii	6.9[c]	Reverse	04 May 2018 22:32:54	−155.000	19.318	5.8
Simeonof, Alaska	7.8	Reverse	22 July 2020 06:12:44	−158.522	55.030	28.0
Chignic, Alaska	8.2	Reverse	29 July 2021 06:15:49	−157.888	55.364	35.0

[a]Magnitudes are from the Global Centroid Moment Tensor (GCMT) catalog. [b]Earthquake origin time and hypocenter location are from the National Research Institute for Earth Science and Disaster Resilience (NIED) for Japan, and from the United States Geological Survey (USGS) for Chile, Mexico, Hawaii, and Alaska earthquakes. [c]Comprehensive analysis by Bai et al. (2018) and Lay et al. (2018) resulted in a magnitude of M_w7.2 for this earthquake.

the magnitude is in the 7.6–7.8 range, a message will indicate a possible tsunami threat to coasts located within 1,000 km of the epicenter. And finally, if the magnitude is greater than M_w7.9, the message will indicate a possible tsunami threat to coasts located within a 3-hr tsunami travel time from the earthquake's epicenter. Different warning criteria have been established for Hawaii ($M_w > 6.9$), Guam, the Virgin Islands, and Puerto Rico ($M_w > 7.1$). The criteria for Samoa depend on location and magnitude.

2. Materials and Methods

2.1. Data Analysis

We gathered collocated GNSS and accelerometer data recorded during nine earthquakes in the magnitude range $7.2 < M_w < 9.1$ that occurred in the Pacific basin offshore Mexico, Chile, Japan, Alaska, and Hawaii (Table 1). Strong-motion and GNSS data for Chile were obtained from the CSN (Báez et al., 2018; Barrientos, 2018). Data for Japan were obtained from the K-net and KiK-net seismic networks (Aoi et al., 2011) operated by the National Research Institute for Earth Science and Disaster Resilience (NIED), and the GEONET GNSS network (Sagiya, 2004; Sagiya et al., 2000). Seismic and GNSS data for Mexico were obtained from both TLALOC-Net and the Servicio Sismológico Nacional (Cabral-Cano et al., 2018). Alaska and Hawaii accelerograms were obtained from the IRIS archive and GNSS data from continuous networks in North America (Murray et al., 2020).

For the purpose of demonstration, we post-processed GNSS phase and pseudorange data, epoch by epoch, to estimate displacements using precise point positioning (PPP) without ambiguity resolution (Ge et al., 2008; Geng et al., 2012), using the International GNSS Service final orbits and Bernese satellite clock estimates (http://www.bernese.unibe.ch/). Similarly precise results can be obtained in real-time using in-receiver or server-based PPP processing. The system that we are testing with PTWC (Figure S1 in Supporting Information S1) uses server-based PPP solutions streamed by UNAVCO's GAGE facility from more than 1,000 Network of the Americas stations (Dittmann et al., 2022; Hodgkinson et al., 2020; Mattioli et al., 2020). The GNSS and accelerometer data were then combined using a seismogeodetic Kalman filter with an acceleration multiplier of 10, as described by Bock et al. (2011) and Saunders et al. (2016), resulting in 100–200 Hz displacement and velocity waveforms (Figure 1).

For calculating earthquake magnitude before the onset of postseismic deformation, it is important to compute the coseismic time window on a station-by-station basis. We adopt the formulation of Golriz et al. (2021) using the seismogeodetic velocity (rather than GNSS displacements which are insensitive to *P*-wave arrivals) to determine the coseismic time window. We used an STA/LTA picker (R. Allen, 1982) to determine the first *P*-wave arrival as the start of the window, and estimate the end time by integrating the normalized velocity squared within a 5 s moving window in time until its 99% point reaches convergence. Movie S1 shows an example of marking the coseismic end time. This process is performed individually for each station, thereby estimating the progression

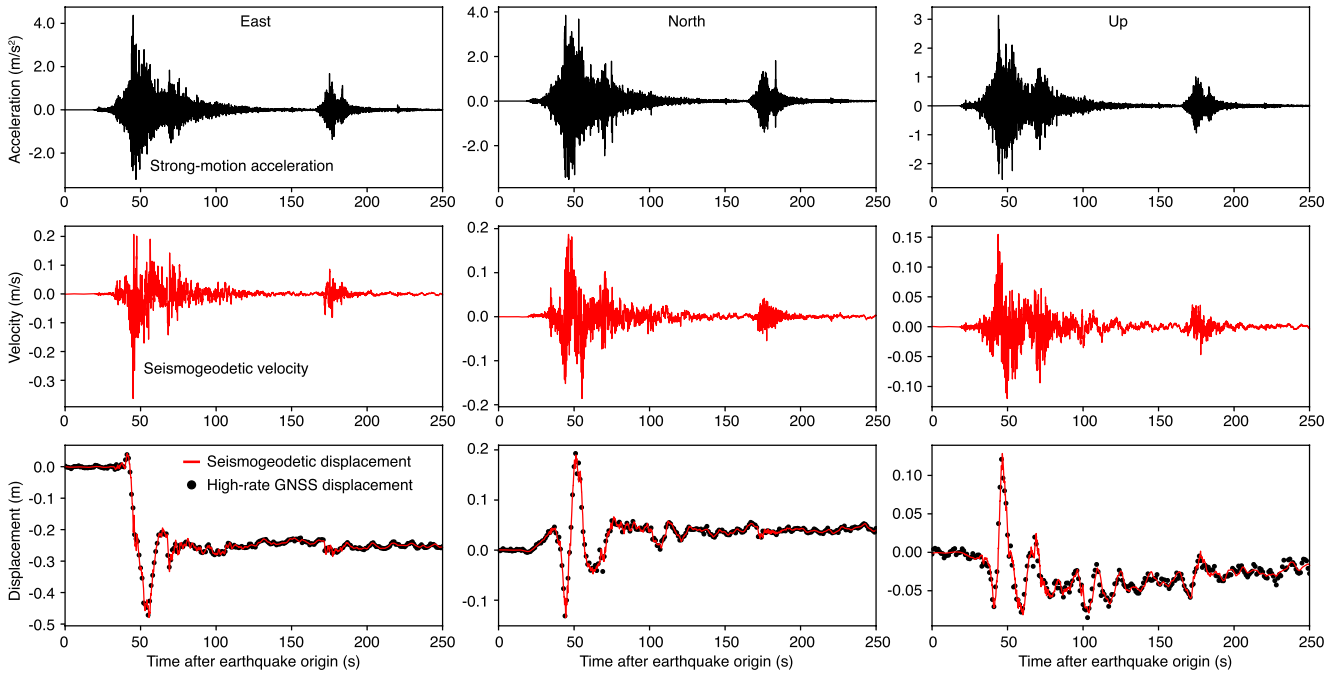

Figure 1. Example of broadband seismogeodetic velocities and displacements recorded during the 2014 M_w8.2 Iquique, Chile earthquake at a site located ~104 km from the hypocenter. The Kalman filter input of strong-motion acceleration (station T08A, top) and high-rate (1 Hz) Global Navigation Satellite Systems (GNSS) displacement (station IQQE, bottom) are in black, while the output of unclipped broadband velocity (middle) and broadband displacement (bottom) are in red.

of the rupture process through the network of sensors. The coseismic window length will vary with epicentral distance, and possibly due to path and site effects. Other source parameters, such as PGDs and static offsets can then be estimated from the displacement waveforms. In this study, we use the coseismic time window to integrate the vertical component of the seismogeodetic displacements (right panels of Movie S1).

2.2. Theory

Aki and Richards (2002) expressed the earthquake displacement field $u\left(\vec{x},t\right)$ generated by a double-couple point source in a homogeneous elastic medium as a sum of near (N), intermediate (IP and IS), and far (FP and FS) field *P*- and *S*-wave terms,

$$\begin{aligned} u\left(\vec{x},t\right) = {} & \frac{A^N}{4\pi\rho r^4}\int_{r/\alpha}^{r/\beta}\tau\, M_0(t-\tau)\,d\tau \\ & + \frac{A^{\mathrm{IP}}}{4\pi\rho\alpha^2 r^2}\, M_0\left(t-\frac{r}{\alpha}\right) + \frac{A^{\mathrm{IS}}}{4\pi\rho\beta^2 r^2}\, M_0\left(t-\frac{r}{\beta}\right) \\ & + \frac{A^{\mathrm{FP}}}{4\pi\rho\alpha^3 r}\,\dot{M}_0\left(t-\frac{r}{\alpha}\right) + \frac{A^{\mathrm{FS}}}{4\pi\rho\beta^3 r}\,\dot{M}_0\left(t-\frac{r}{\beta}\right), \end{aligned} \tag{1}$$

where r is the distance between source and receiver, t is time, the A^i terms represent the radiation patterns, and ρ, α, and β are the density, *P*-wave, and *S*-wave velocities, respectively. $M_0(t)$ is the time history of the seismic moment, and its derivative, $\dot{M}_0(t)$, is the moment rate. Left side of the equation (u, displacement) and the first term (of N) would be on the first line, the second and third terms (of IP and IS) would be on the second line, and the fourth and the fifth terms (of FP and FS) would be on the third line.All five terms are separated by the plus (+) sign.

Since the *P*-wave is most pronounced in the vertical direction, we follow Kikuchi and Ishida (1993) and Tsuboi et al. (1995) and use the vertical component of seismogeodetic displacement (as justified in Section 3), $u_z\left(\vec{x},t\right)$, limited to the far-field *P*-wave term, as an approximate moment rate function

$$u_z\left(\vec{x},t\right) = \frac{A^{\mathrm{FP}}}{4\pi\rho\alpha^3 r}\,\dot{M}_0\left(t-\frac{r}{\alpha}\right), \tag{2}$$

where A^{FP} represents the radiation pattern generated by a double-couple source.

We estimate the seismic moment by integrating $u\left(\vec{x},t\right)$ in Equation 2. Because the real Earth is heterogenous, $u\left(\vec{x},t\right)$ contains path (attenuation and geometrical spreading) and receiver (free surface response at the station) effects. We apply approximations to account for these effects following Tsuboi et al. (1995), and assume values of 0.8 for anelastic attenuation, $1.2r$ for geometrical spreading, and 1.5 for the free surface effect at the receiver.

We integrate $u_z\left(\vec{x},t\right)$ to obtain the moment history, $M_0(t)$, at each station

$$M_0(t) = \frac{4\pi\rho\alpha^3 r}{A^{FP}} \int u_z\left(\vec{x},t\right) dt. \tag{3}$$

By using seismogeodetic displacement, instead of seismic velocity, we avoid doubly integrating velocities to estimate $M_0(t)$, thereby reducing baseline errors (Melgar, Bock, et al., 2013). Assuming that the maximum absolute value of the moment function in Equation 3 recorded at each station is the actual seismic moment of the earthquake, M_0, we follow Tsuboi et al. (1995) by estimating

$$M_0 \cong 4\pi\rho\alpha^3 r \,\mathrm{Max}\left| \int u_z\left(\vec{x},t\right) dt \right|. \tag{4}$$

Tsuboi et al. (1995) showed that a combination of multiple records will give a good estimate of M_0 without correcting for A^{FP}, assuming a reasonable azimuthal coverage. Therefore, in this study we do not correct for this term. For the other parameters in Equation 4, we choose representative values for the uppermost mantle of $\rho = 3400\,\mathrm{kg/m^3}$ and $\alpha = 7900\,\mathrm{m/s}$ (Tsuboi et al., 1995). As indicated earlier, we determine the coseismic time window for the integration in Equation 4 at each station individually using the seismogeodetic velocity (Golriz et al., 2021). We then compute the seismogeodetic moment magnitude at each station, following Kanamori (1977)

$$M_{wg} = \frac{2}{3}\left(\log_{10} M_0 - 9.1\right) \tag{5}$$

which we refer to as M_{wg} to distinguish it from a magnitude estimate derived solely from seismic data.

Figure 2 shows an example of a vertical seismogeodetic displacement time series and the derived moment function for collocated seismic and GNSS stations recorded during the 2011 M_w9.1 Tohoku-Oki, Japan earthquake. The final coseismic time window (top panel) is denoted by the vertical lines. The time of detected peaks in the moment function (bottom panel, gray and red circles) together with the end time of the coseismic window indicate that we can derive/calculate a reliable magnitude estimate within ~180 s (before the end of the rupture) and a more accurate final estimate within ~300 s after origin time. Our estimates of the seismic moment are based directly on the maximum value of integrated displacement. Thus, regression against other source parameters such as PGD versus distance (Crowell et al., 2013), empirically based on the historical record, is not required. Movie S1 provides another example of the process of estimating the coseismic window and seismogeodetic magnitude.

3. Results and Discussion

We use vertical displacement $u_z\left(\vec{x},t\right)$ from nine dip-slip earthquakes (eight thrust faulting and one normal faulting) in the $7.2 < M_w < 9.1$ range to estimate seismic moment and seismogeodetic moment magnitude, M_{wg}, for each earthquake. Once the P-wave is detected, we calculate the magnitude at 5-s intervals, for each station in parallel using Equations 4 and 5. The final magnitude for a given station is reported at the end time of its coseismic window. In Figure 3, we present the magnitude estimate evolution over time after rupture initiation for each earthquake, with individual station estimates shown as gray curves and the event medians (more robust than means) every 10-s shown as red scatter points with error bars estimated as ±1 interquartile-range (IQR) of all station estimates. The IQR is defined as the range of the middle 50% of the data, the difference between the 75th and 25th percentiles. When a data sample is drawn from a normal distribution, its mean very nearly equals its median and its standard deviation equals about three quarters of the IQR.

The estimated M_{wg} magnitudes are within ±0.15 magnitude units of the GCMT M_w values (Dziewonski et al., 1981; Ekström et al., 2012) and within their IQR uncertainties for the seven shallow thrust events of

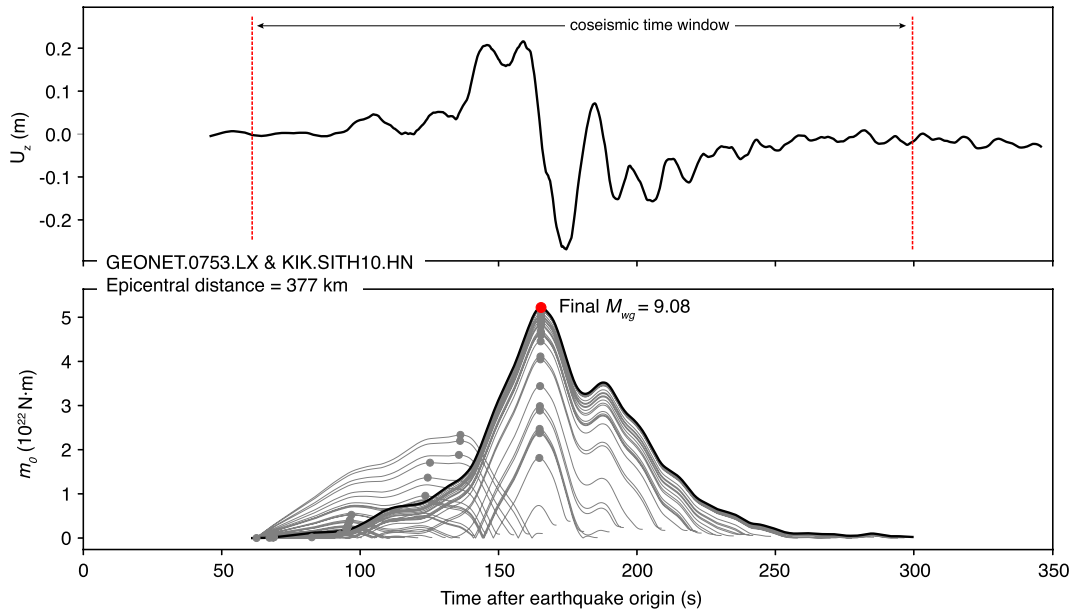

Figure 2. Example of vertical seismogeodetic displacement (top), and the derived moment function within the evolving coseismic window (bottom) for a collocated station during the 2011 M_w9.1 Tohoku-Oki, Japan earthquake. The final coseismic time window is denoted by the vertical lines (top), and its derived final moment function in black (bottom) with the maximum value as a red point. The reported final seismogeodetic moment magnitude estimate for this station is based on Equations 4 and 5.

$M_w > 7.8$. We estimate M_{wg}8.52 compared to the GCMT of M_w8.2 for the 2017 Chiapas event. Note that this is the only event with a normal fault mechanism while all the others are thrust events. The closest station (~70 km) recording during the 2020 M_w7.8 Simeonof earthquake overestimates the magnitude with M_{wg}8.51 and is clearly an outlier. This station lies in close proximity to the trench and experienced ~33 cm of coseismic uplift. Therefore, our far-field assumption (Equation 2) may not be valid in this case or the discrepancy may be due to directivity or site effects. Nevertheless, the event median of M_{wg}7.84 matches the final published magnitude. Our estimate of M_{wg}7.38 for the 2018 Kilauea, Hawaii earthquake is significantly larger than the GCMT value of M_w6.9. However, because of the inverse relationship between dip and seismic moment for shallow earthquakes, the magnitude of the 2018 Kilauea event is likely closer to M_w7.2 (Bai et al., 2018; Lay et al., 2018; Liu et al., 2018), in closer agreement with our results. In addition, the low rupture velocity (~1 km/s), long rupture duration (~40 s), and low moment-scaled radiated energy, imply frictional properties similar to those in the shallow portions of subduction zones where tsunami earthquakes occur (Liu et al., 2018). If that is the case here, our results (albeit from a sample of a single event) suggest that we can get an accurate magnitude estimate for tsunami earthquakes.

To justify our use of only the far field vertical *P*-wave component (FP) of the earthquake displacement field $u\left(\vec{x},t\right)$, we follow Madariaga et al. (2019) and express the near-field (first) term (N) of Equation 1 in a slightly different form,

$$\frac{A^N}{4\pi\rho\beta^2 r^2}\int_{\beta/\alpha}^{1}\tau\, M_0\left(\frac{\beta t}{r}-\tau\right)d\tau. \tag{6}$$

and show that the near-field displacement term falls off as r^{-2}. Since the intermediate-field displacement terms also fall off as r^{-2}, the near- and intermediate-field (NF and IF) terms are not separable by studying their radiation; they combine to produce a coseismic static offset which attenuates at r^{-2} compared to the r^{-1} decay of the (dynamic) far-field terms (Madariaga et al., 2019; Nikolaidis et al., 2001). By estimating the permanent coseismic displacement offset (NF + IF terms) and subtracting it from the vertical PGD (NF + IF + FF terms), we determine the displacement due to the (dynamic) far-field (FF) term only. For the largest earthquake in our data set (2011 M_w9.1 Tohoku-Oki), the far-field terms dominate the vertical component of displacement beyond

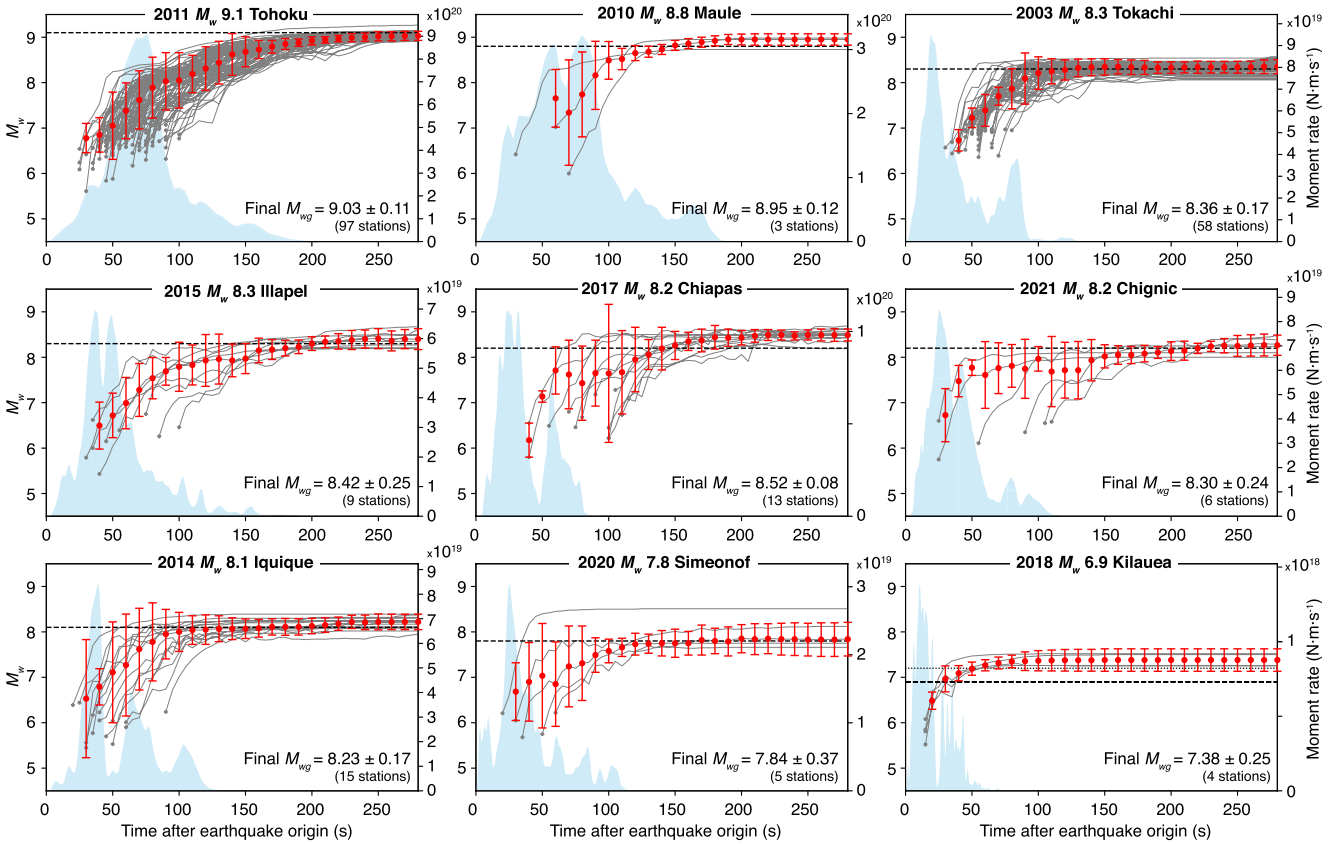

Figure 3. Time evolution of our magnitude estimates for nine earthquakes used in this study. Gray curves denote individual stations, red points are event medians with ±1 interquartile-range. Moment rate functions from the United States Geological Survey are in light blue. The Global Centroid Moment Tensor magnitudes are denoted by black dashed horizontal lines. For the 2018 Kilauea event, we also include a black dotted line indicating the M_w7.2 estimate of Bai et al. (2018) and Lay et al. (2018).

$r \sim 175$ km epicentral distance (Figure 4) which, for this bilaterally rupturing event, corresponds to ~½ of its rupture length of ~350 km (Hayes, 2017; Ye et al., 2016). This result justifies the use of the far-field *P*-wave term of Equation 1. Also, for steeper incident rays at the receiving sites, the longitudinal (radial) energy, mostly *P*- with very little vertically polarized *S*-waves, would dominate on the vertical components (with very little, if any, horizontally polarized *S*-waves). This justifies using the *P*-wave term recorded by the vertical component.

Because we integrate the vertical component of displacement over the entire coseismic window, we are able to measure the largest moment release even if it occurs after an earlier but smaller peak. This provides accurate M_{wg} estimates for complex earthquakes as well as for tsunami earthquakes where peak moment release may occur late enough in the rupture process to indicate a long rupture duration. Therefore, the time of the maximum peak as well as its amplitude should allow identification of tsunami earthquakes.

We compare our M_{wg} approach with two additional magnitude determination methods that rely on high-rate GNSS displacements; the empirical PGD scaling law (M_{pgd}), and W-phase inversion from regional GNSS (M_{ww}). For the M_{pgd} calculation and regression, we use all available GNSS stations (instead of collocated only) and follow the procedure described at Ruhl et al. (2019). We set a minimum PGD value of 3 cm, a maximum hypocentral distance of 1,000 km, and signal-to-noise ratio of 3 and above for a station to be included in the regression. The PGD versus hypocentral distance regressions are shown in Figure S1 in Supporting Information S1. The GNSS-derived W-phase results of M_{ww} are taken from Riquelme et al. (2016) and only available for the 2010 M_w8.8 Maule, 2011 M_w9.1 Tohoku, 2014 M_w8.1 Iquique, and 2015 M_w8.3 Illapel earthquakes. We compare final results of the three methods in Table 2, and a timeline for the first 5 min after earthquake origin time in Figure S3 in Supporting Information S1. The uncertainty for M_{wg} is defined as ±1 IQR, similar to error bars on Figure 3, while the uncertainty for M_{pgd} is defined as the root mean square error of the linear regression.

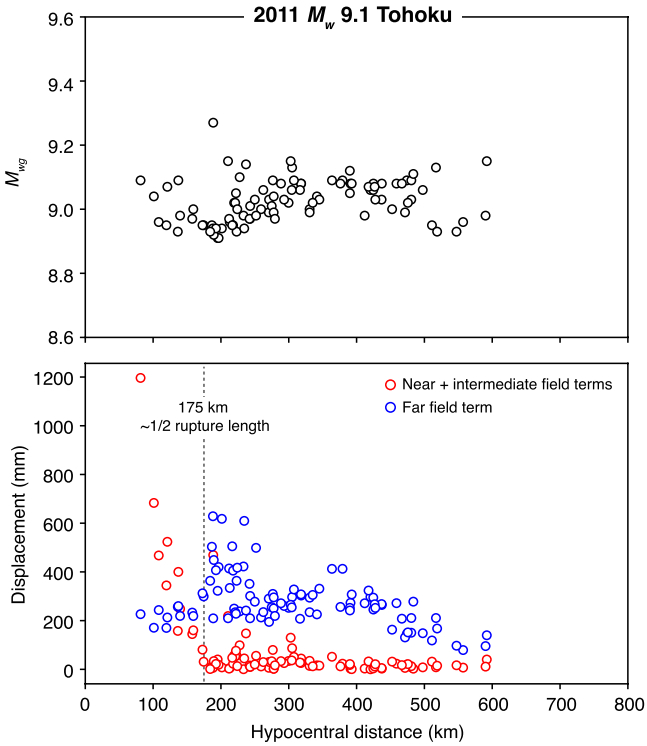

Figure 4. Distinguishing the contribution of far-field vertical displacements in Equation 1 for the 2011 M_w9.1 Tohoku-Oki earthquake. Top: records of estimated M_{wg} per station as a function of epicentral distance. Bottom: absolute value of permanent vertical coseismic offsets (near- and intermediate-field terms) as red points, and the difference between vertical peak displacements and static offsets (far-field term) as blue points, as a function of epicentral distance. Note that the FF *P*-waves dominate the vertical component of displacement beyond ~175 km epicentral distance.

No M_{ww} uncertainty was reported at Riquelme et al. (2016). Six of the nine events are earthquakes used by Ruhl et al. (2019) in their PGD regressions. The M_{pgd} magnitudes for two of the "new" earthquakes (i.e., not included in the published analysis), 2020 M_w7.8 Simeonof and 2021 M_w8.2 Chignic, are underestimated compared to the GCMT and M_{wg} magnitudes, which match within the uncertainties of M_{wg}. For the 2018 Kilauea earthquake, M_{pgd} (6.67 ± 0.15) is closer to M_w6.9 while M_{wg} (7.38 ± 0.25) is significantly overestimated. However, as indicated earlier, our results are consistent with the analysis by Bai et al. (2018) and Lay et al. (2018) who estimate a magnitude of M_w7.2 for the 2018 Kilauea event. Furthermore, using the Ruhl et al. (2019) regression coefficients results in a significant underestimate of the 2014 M_w8.1 Iquique and 2015 M_w8.3 Illapel earthquake magnitudes (Table 2). The M_{wg} estimates are more accurate than M_{pgd} except for the single normal event in our data set, the 2017 Chiapas earthquake, where M_{wg} is a significant overestimate. Therefore, even though PGD-based magnitude estimates are timelier (Figure S3 in Supporting Information S1) and despite our study being limited to nine earthquakes, our theory-based seismogeodetic M_{wg} results are accurate and valuable estimates of M_w. Although beyond the scope of this study, we speculate that the empirically based PGD method insufficiently accounts for the full range of source, site and/or path effects. GNSS-derived W-phase final (within 4–5 min) results of M_{ww} are comparable to our M_{wg} estimates for the four earthquakes reported by Riquelme et al. (2016). W-phase inversion is stable within 4–5 min after rupture initiation for most cases. Using the M_{wg} approach, initial estimates of M_w7+ are available within 1 min and could be beneficial for early tsunami threat messages. It is important to note that M_{ww} inversion includes earthquake focal mechanism, which is a key component for the assessment of tsunamigenic potential.

We neglected the radiation pattern term A^{FP} term in Equation 1 based on Tsuboi et al. (1995), who showed that a combination of multiple records will give a good estimate of M_w, assuming a reasonable azimuthal coverage. We assumed a value of 1 for the A^{FP} term in Equations 2 and 3. Assuming an extreme case of $A^{FP} = 0.1$, this term will lead to a 2/3 (0.67) of a magnitude unit difference in our M_{wg} estimate for a particular station resulting in an increased magnitude. However, we do not expect this term to vary significantly from 1 within on-shore stations during a thrust faulting event. In fact, Tsuboi et al. (1995) showed that the

Table 2
Comparison Between Global Navigation Satellite Systems-Based M_w Estimates

		M_{wg}		M_{pgd}		M_{ww}	
Name/Region	M_w	Estimate	#Stations	Estimate	#Stations	Estimate	#Stations
Tokachi-Oki, Japan	8.3	8.36 ± 0.17	58	7.96 ± 0.20	307	–	–
Maule, Chile	8.8	8.95 ± 0.12	3	8.92 ± 0.09	19	8.90	12
Tohoku-Oki, Japan	9.1	9.03 ± 0.11	97	9.14 ± 0.15	916	9.00	375
Iquique, Chile	8.1	8.23 ± 0.17	15	7.59 ± 0.20	21	8.10	9
Illapel, Chile	8.3	8.42 ± 0.25	9	7.68 ± 0.30	35	8.40	15
Chiapas, Mexico	8.2	8.52 ± 0.08	13	8.24 ± 0.21	27	–	–
Kilauea, Hawaii	6.9[a]	7.38 ± 0.25	4	6.68 ± 0.15	15	–	–
Simeonof, Alaska	7.8	7.84 ± 0.37	5	7.47 ± 0.12	18	–	–
Chignic, Alaska	8.2	8.30 ± 0.24	6	7.70 ± 0.21	43	–	–

Note. M_{wg} (This Study), M_{pgd} (Following Ruhl et al., 2019), and M_{ww} (Taken From Riquelme et al., 2016).
[a]Comprehensive analysis by Bai et al. (2018) and Lay et al. (2018) resulted in a magnitude of M_w7.2 for this earthquake.

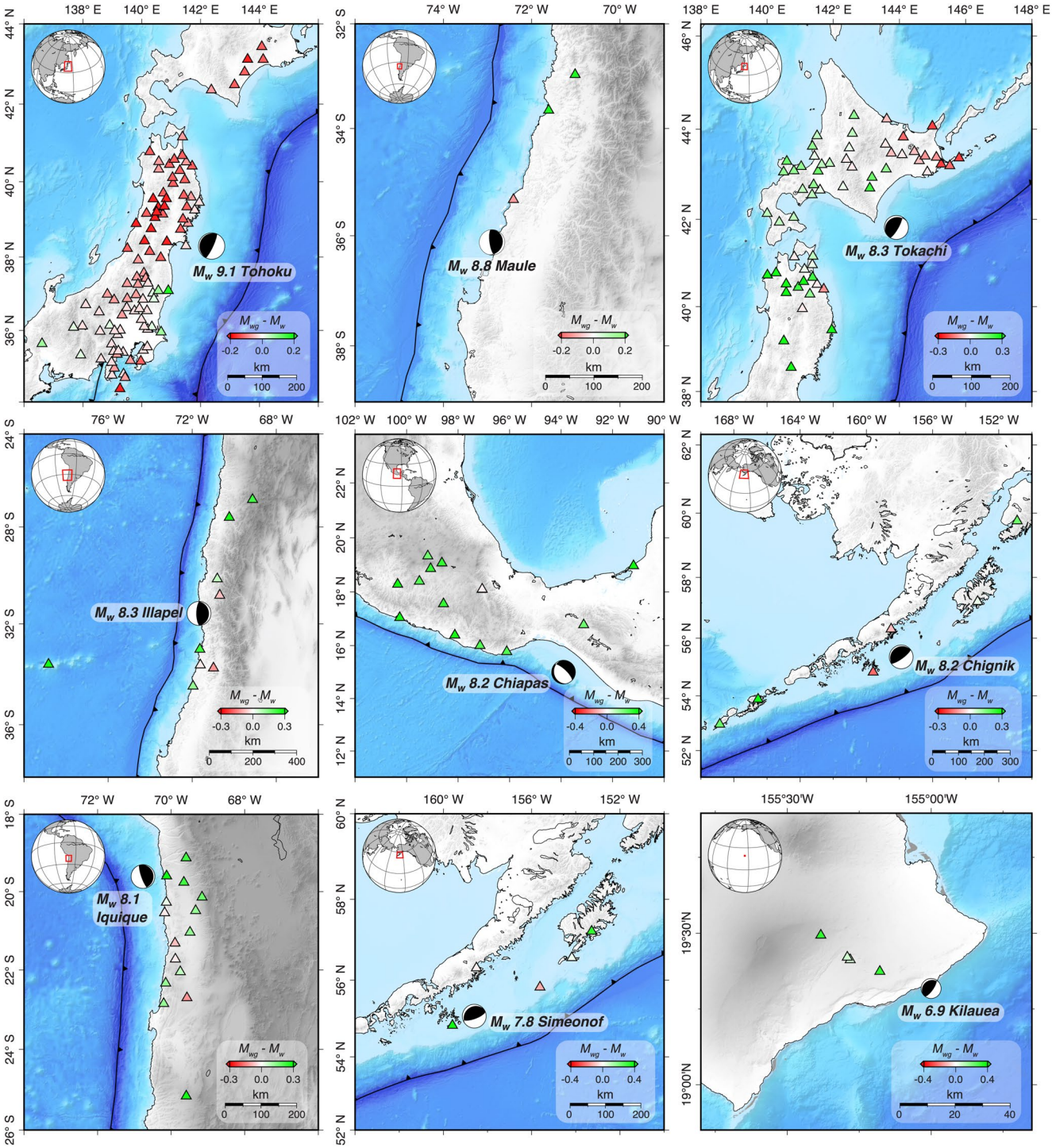

Figure 5. Spatial distribution of station by station M_{wg} estimates for all earthquakes included in our study. Green colors indicate overestimates, while red colors indicate underestimates.

averaged radiation pattern over the entire focal sphere is $\overline{A^{FP}} \cong \sqrt{4/15}$, which is, based on Equations 3 and 5, equivalent to 0.2 magnitude units. Due to the nature of subduction zones and the land-based GNSS and seismic instrumentation, most earthquakes in our data set are associated with azimuthal gaps larger than 180° (Goldberg & Bock, 2017). This is particularly of concern for the Kilauea, Iquique, and Chiapas earthquakes. Therefore, we explored the effect of the spatial distribution of the stations on the estimated magnitude (Figure 5). We find that

M_{wg} provides precise and accurate magnitude estimates for tsunamigenic earthquakes even with poor azimuthal or sparse station coverage (e.g., the three stations for the 2010 M_w8.8 Maule earthquake).

Improvements may still be obtained by considering the radiation patterns in Equation 1. However, one must assume, a priori, a focal mechanism in order to calculate them. The focal mechanisms from *P*-wave polarities can be estimated in real-time. However, these give only the focal mechanism for the initial rupture at the epicenter and can often be significantly different from the final focal mechanism. For real-time purposes, one can assume that rupture occurs down-dip of the trench and use a generalized thrust focal mechanism as an input for radiation pattern term calculations. We are also exploring the introduction of a regional velocity model and a rapid finite fault slip inversion from the seismogeodetic or GNSS-only displacements to take into account the radiation pattern.

We continue to test M_{wg} estimation with a seismogeodetic approach extended for interleaved high-rate GNSS and seismic instruments that may only have a subset of collocated stations. This scenario requires spatial interpolation of the coseismic time window from regional seismic stations to the GNSS stations, as demonstrated by Golriz et al. (2021). Since most local tsunamis are caused by thrust events, we have not considered strike-slip fault mechanisms in this study although this is certainly of interest for rapid magnitude estimation for earthquake early warning systems such as ShakeAlert (Given et al., 2014; Kohler et al., 2020) in the U.S. West Coast, which includes major strike-slip fault regimes. For that purpose, one should account for the other (*S*-wave) terms in Equation 1 and use the horizontal seismogeodetic components to obtain a reliable estimate for strike-slip earthquakes.

4. Conclusions

We present a seismogeodetic approach to rapid magnitude estimation based on the method developed for broadband seismic data by Tsuboi et al. (1995) and using the far-field *P*-wave term in the representation of the displacement field as a point source in a spherically homogeneous medium (Aki & Richards, 2002). Our approach is earthquake specific in contrast to empirical methods that rely on historical earthquake records. By combining high-rate GNSS displacements with strong-motion accelerations at collocated stations, we estimate broadband seismogeodetic displacement and velocity waveforms and circumvent limitations associated with double-integration of regional-to-teleseismic broadband velocity, triple-integration of accelerations, and less precise (and lower rate) GNSS data only. We demonstrate the M_{wg} approach using nine tsunamigenic earthquakes in the Pacific basin with $7.2 < M_w < 9.1$. We are able to estimate station-by-station moment magnitude using the vertical component of displacement with a precision of 0.18 magnitude units for eight thrust faulting events and 0.32 magnitude units for a single normal faulting event, within 2–3 min of onset time for the set of earthquakes in this study. In general, the latency will vary with different source time functions. These results indicate that our approach is particularly well suited to local tsunami warning systems where response time is essential and to rapid analysis of tsunami earthquakes with complex fault mechanisms. Therefore, we advocate for a large-scale seismogeodetic network expansion to mitigate the risks to vulnerable populations and infrastructure.

Conflict of Interest

The authors declare no conflicts of interest relevant to this study.

Data Availability Statement

High-rate GNSS displacement and seismogeodetic data for historical earthquakes are available from the Scripps Institution of Oceanography's Orbit and Permanent Array Center (SOPAC) and Caltech's Jet Propulsion Laboratory (JPL) MEaSUREs project, NASA # NNH17ZDA001N-MEaSUREs project (Bock et al., 2021, http://garner.ucsd.edu/pub/measuresESESES_products/ATBD/ESESES-ATBD.pdf). The data can be found at SOPAC (http://garner.ucsd.edu/pub/measuresESESES_products/EarthquakeDisplacements/—username: anonymous; password: your email) and at NASA's EARTHDATA web portal (https://cddis.nasa.gov/archive/GPS_Explorer/archive/earthquake_displacements/—users must create an Earthdata login). More details on the archive of historical seismogeodetic and high-rate GNSS displacements can be found at http://sopac-csrc.ucsd.edu/index.php/highrategnss/. The Hawaii island 50 m resolution bathymetry data set is available for download from: http://

www.soest.hawaii.edu/hmrg/multibeam/bathymetry.php. Topography and bathymetry data for the other regions are from Tozer et al. (2019).

Acknowledgments
This research was made possible by data products provided by the NASA NNH17ZDA001N-MEaSUREs project. Several figures were made using the Generic Mapping Tools (Wessel et al., 2013). We would like to thank two anonymous reviewers and the editor, Satoshi Ide, for their useful feedback that helped us improve this manuscript.

References

Aki, K., & Richards, P. G. (2002). Quantitative seismology.

Allen, R. (1982). Automatic phase pickers: Their present use and future prospects. *Bulletin of the Seismological Society of America*, *72*(6B), S225–S242. https://doi.org/10.1785/BSSA07206B0225

Allen, R. V. (1978). Automatic earthquake recognition and timing from single traces. *Bulletin of the Seismological Society of America*, *68*(5), 1521–1532. https://doi.org/10.1785/BSSA0680051521

Aoi, S., Kunugi, T., Nakamura, H., & Fujiwara, H. (2011). Deployment of new strong motion seismographs of K-NET and KiK-net. In *Earthquake data in engineering seismology* (pp. 167–186). Springer. https://doi.org/10.1186/s40623-017-0604-8

Báez, J. C., Leyton, F., Troncoso, C., del Campo, F., Bevis, M., Vigny, C., et al. (2018). The Chilean GNSS network: Current status and progress toward early warning applications. *Seismological Research Letters*, *89*(4), 1546–1554. https://doi.org/10.1785/0220180011

Bai, Y., Ye, L., Yamazaki, Y., Lay, T., & Cheung, K. F. (2018). The 4 May 2018 MW 6.9 Hawaii Island earthquake and implications for tsunami hazards. *Geophysical Research Letters*, *45*(20), 11–040. https://doi.org/10.1029/2018GL079742

Barrientos, S., & National Seismological Center CSN Team. (2018). The seismic network of Chile. *Seismological Research Letters*, *89*(2A), 467–474. https://doi.org/10.1785/0220160195

Blewitt, G., Kreemer, C., Hammond, W. C., Plag, H. P., Stein, S., & Okal, E. (2006). Rapid determination of earthquake magnitude using GPS for tsunami warning systems. *Geophysical Research Letters*, *33*(11), 2006GL026145. https://doi.org/10.1029/2006gl026145

Bock, Y., Melgar, D., & Crowell, B. W. (2011). Real-time strong-motion broadband displacements from collocated GPS and accelerometers. *Bulletin of the Seismological Society of America*, *101*(6), 2904–2925. https://doi.org/10.1785/0120110007

Bock, Y., Moore, A. W., Argus, D., Fang, P., Golriz, D., Guns, K., et al. (2021). Extended Solid Earth science ESDR system (ES3): Algorithm theoretical basis document, Sept. 19, NASA MEaSUREs project #NNH17ZDA001N. Retrieved from http://garner.ucsd.edu/pub/measuresESESES_products/ATBD/ESESES-ATBD.pdf

Bock, Y., Nikolaidis, R. M., de Jonge, P. J., & Bevis, M. (2000). Instantaneous geodetic positioning at medium distances with the Global Positioning System. *Journal of Geophysical Research*, *105*(B12), 28223–28253. https://doi.org/10.1029/2000jb900268

Bock, Y., Prawirodirdjo, L., & Melbourne, T. I. (2004). Detection of arbitrarily large dynamic ground motions with a dense high-rate GPS network. *Geophysical Research Letters*, *31*(6), L06604. https://doi.org/10.1029/2003gl019150

Boore, D. M. (2001). Effect of baseline corrections on displacements and response spectra for several recordings of the 1999 Chi-Chi, Taiwan, earthquake. *Bulletin of the Seismological Society of America*, *91*(5), 1199–1211. https://doi.org/10.1785/0120000703

Boore, D. M., Stephens, C. D., & Joyner, W. B. (2002). Comments on baseline correction of digital strong-motion data: Examples from the 1999 Hector Mine, California, earthquake. *Bulletin of the Seismological Society of America*, *92*(4), 1543–1560. https://doi.org/10.1785/0120000926

Bryant, E. (2008). *Tsunami: The underrated hazard*. Springer.

Cabral-Cano, E., Pérez-Campos, X., Márquez-Azúa, B., Sergeeva, M. A., Salazar-Tlaczani, L., DeMets, C., et al. (2018). TLALOCNet: A continuous GPS-met backbone in Mexico for seismotectonic and atmospheric research. *Seismological Research Letters*, *89*(2A), 373–381. https://doi.org/10.1785/0220170190

Crowell, B. W., Melgar, D., Bock, Y., Haase, J. S., & Geng, J. (2013). Earthquake magnitude scaling using seismogeodetic data. *Geophysical Research Letters*, *40*(23), 6089–6094. https://doi.org/10.1002/2013GL058391

Crowell, B. W., Schmidt, D. A., Bodin, P., Vidale, J. E., Baker, B., Barrientos, S., & Geng, J. (2018). G-FAST earthquake early warning potential for great earthquakes in Chile. *Seismological Research Letters*, *89*(2A), 542–556. https://doi.org/10.1785/0220170180

Dittmann, T., Hodgkinson, K., Morton, J., Mencin, D., & Mattioli, G. S. (2022). Comparing sensitivities of geodetic processing methods for rapid earthquake magnitude estimation. *Seismological Society of America*, *93*(3), 1497–1509. https://doi.org/10.1785/0220210265

Dziewonski, A. M., Chou, T.-A., & Woodhouse, J. H. (1981). Determination of earthquake source parameter from waveform data for studies of global and regional seismicity. *Journal of Geophysical Research*, *86*(B4), 2825–2852. https://doi.org/10.1029/JB086iB04p02825

Ekström, G., Nettles, M., & Dziewoński, A. M. (2012). The global CMT project 2004–2010: Centroid-moment tensors for 13,017 earthquakes. *Physics of the Earth and Planetary Interiors*, *200*, 1–9. https://doi.org/10.1016/j.pepi.2012.04.002

Elbanna, A., Abdelmeguid, M., Ma, X., Amlani, F., Bhat, H. S., Synolakis, C., & Rosakis, A. J. (2021). Anatomy of strike-slip fault tsunami Genesis. *Proceedings of the National Academy of Sciences of the United States of America*, *118*(19), e2025632118. https://doi.org/10.1073/pnas.2025632118

Emore, G. L., Haase, J. S., Choi, K., Larson, K. M., & Yamagiwa, A. (2007). Recovering seismic displacements through combined use of 1-Hz GPS and strong-motion accelerometers. *Bulletin of the Seismological Society of America*, *97*(2), 357–378. https://doi.org/10.1785/0120060153

Evans, J. R., & Allen, S. S. (1983). A teleseism-specific detection algorithm for single short-period traces. *Bulletin of the Seismological Society of America*, *73*(4), 1173–1186. https://doi.org/10.1785/BSSA0730041173

Ge, M., Gendt, G., Rothacher, M. A., Shi, C., & Liu, J. (2008). Resolution of GPS carrier-phase ambiguities in precise point positioning (PPP) with daily observations. *Journal of Geodesy*, *82*(7), 389–399. https://doi.org/10.1007/s00190-007-0187-4

Geng, J., Shi, C., Ge, M., Dodson, A. H., Lou, Y., Zhao, Q., & Liu, J. (2012). Improving the estimation of fractional-cycle biases for ambiguity resolution in precise point positioning. *Journal of Geodesy*, *86*(8), 579–589. https://doi.org/10.1007/s00190-011-0537-0

Genrich, J. F., & Bock, Y. (2006). Instantaneous geodetic positioning with 10–50 Hz GPS measurements: Noise characteristics and implications for monitoring networks. *Journal of Geophysical Research*, *111*(B3), B03403. https://doi.org/10.1029/2005jb003617

Given, D. D., Cochran, E. S., Heaton, T., Hauksson, E., Allen, R., Hellweg, P., et al. (2014). *Technical implementation plan for the ShakeAlert production system: An earthquake early warning system for the west coast of the United States*, Open-File Report 2014–1097. U.S. Department of the Interior, U.S. Geological Survey.

Goldberg, D. E., & Bock, Y. (2017). Self-contained local broadband seismogeodetic early warning system: Detection and location. *Journal of Geophysical Research: Solid Earth*, *122*(4), 3197–3220. https://doi.org/10.1002/2016JB013766

Golriz, D., Bock, Y., & Xu, X. (2021). Defining the coseismic phase of the crustal deformation cycle with seismogeodesy. *Journal of Geophysical Research: Solid Earth*, *126*(10), e2021JB022002. https://doi.org/10.1029/2021JB022002

Graizer, V. M. (1979). Determination of the true ground displacement by using strong motion records. *Izvestiya USSR Academy of Sciences, Physics Solid Earth*, *15*, 875–885.

Grapenthin, R., Johanson, I. A., & Allen, R. M. (2014). Operational real-time GPS-enhanced earthquake early warning. *Journal of Geophysical Research: Solid Earth*, *119*(10), 7944–7965. https://doi.org/10.1002/2014jb011400

Hayes, G. P. (2017). The finite, kinematic rupture properties of great-sized earthquakes since 1990. *Earth and Planetary Science Letters*, *468*, 94–100. https://doi.org/10.1016/j.epsl.2017.04.003

Hirshorn, B. (2007). The Pacific tsunami warning center response to the M_w6. 7 Kiholo Bay earthquake and lessons for the future. *Seismological Research Letters*, *78*, 299.

Hirshorn, B., & Weinstein, S. (2009). Rapid estimates of earthquake source parameters for tsunami warning. In A. Meyers (Ed.), *Encyclopedia of complexity and systems science*, (p. 10370). Springer. https://doi.org/10.1007/978-0-387-30440-3_160

Hirshorn, B., Weinstein, S., Wang, D., Koyanagi, K., Becker, N., & McCreery, C. (2019). Earthquake source parameters, rapid estimates for tsunami forecasts and warnings. In R. Meyers (Ed.), *Encyclopedia of complexity and systems science*. Springer. https://doi.org/10.1007/978-3-642-27737-5_160-2

Hodgkinson, K. M., Mencin, D. J., Feaux, K., Sievers, C., & Mattioli, G. S. (2020). Evaluation of earthquake magnitude estimation and event detection thresholds for real-time GNSS networks: Examples from recent events captured by the network of the Americas. *Seismological Research Letters*, *91*(3), 1628–1645. https://doi.org/10.1785/0220190269

Hoshiba, M., & Ozaki, T. (2014). Earthquake early warning and tsunami warning of the Japan Meteorological Agency, and their performance in the 2011 off the Pacific coast of Tohoku earthquake (M_w9.0). In *Early warning for geological disasters* (pp. 1–28). Springer. https://doi.org/10.1007/978-3-642-12233-0_1

Iwan, W. D., Moser, M. A., & Peng, C. Y. (1985). Some observations on strong-motion earthquake measurement using a digital accelerograph. *Bulletin of the Seismological Society of America*, *75*(5), 1225–1246. https://doi.org/10.1785/BSSA0750051225

Johnson, C. E., Bittenbinder, A., Bogaert, B., Dietz, L., & Kohler, W. (1995). Earthworm: A flexible approach to seismic network processing. *Iris newsletter*, *14*(2), 1–4.

Johnson, C. E., Lindh, A., & Hirshorn, B. (1997). Robust regional phase association (pp. 94–621). USGS Open File Report. https://doi.org/10.3133/ofr94621

Kanamori, H. (1972). Mechanism of tsunami earthquakes. *Physics of the Earth and Planetary Interiors*, *6*(5), 346–359. https://doi.org/10.1016/0031-9201(72)90058-1

Kanamori, H. (1977). The energy release in great earthquakes. *Journal of Geophysical Research*, *82*(20), 2981–2987. https://doi.org/10.1029/JB082i020p02981

Kanamori, H. (1993). W phase. *Geophysical Research Letters*, *20*(16), 1691–1694. https://doi.org/10.1029/93GL01883

Kanamori, H., & Rivera, L. (2008). Source inversion of W phase: Speeding up seismic tsunami warning. *Geophysics Journal International*, *175*(1), 222–238. https://doi.org/10.1111/j.1365246X.2008.03887.x

Käufl, P., Valentine, A. P., O'Toole, T. B., & Trampert, J. (2014). A framework for fast probabilistic centroid-moment-tensor determination—Inversion of regional static displacement measurements. *Geophysical Journal International*, *196*(3), 1676–1693. https://doi.org/10.1093/gji/ggt473

Kawamoto, S., Hiyama, Y., Ohta, Y., & Nishimura, T. (2016). First result from the GEONET real-time analysis system (REGARD): The case of the 2016 Kumamoto earthquakes. *Earth Planets and Space*, *68*(1), 1–12. https://doi.org/10.1186/s40623-016-0564-4

Kido, M., Osada, Y., Fujimoto, H., Hino, R., & Ito, Y. (2011). Trench-normal variation in observed seafloor displacements associated with the 2011 Tohoku-Oki earthquake. *Geophysical Research Letters*, *38*(24), L24303. https://doi.org/10.1029/2011GL050057

Kikuchi, M., & Ishida, M. (1993). Source retrieval for deep local earthquakes with broadband records. *Bulletin of the Seismological Society of America*, *83*(6), 1855–1870. https://doi.org/10.1785/BSSA0830061855

Kohler, M. D., Smith, D. E., Andrews, J., Chung, A. I., Hartog, R., Henson, I., et al. (2020). Earthquake early warning ShakeAlert 2.0: Public rollout. *Seismological Research Letters*, *91*(3), 1763–1775. https://doi.org/10.1785/0220190245

Langbein, J., Borcherdt, R., Dreger, D., Fletcher, J., Hardebeck, J. L., Hellweg, M., et al. (2005). Preliminary report on the 28 September 2004, M 6.0 Parkfield, California earthquake. *Seismological Research Letters*, *76*(1), 10–26. https://doi.org/10.1785/gssrl.76.1.10

Larson, K. M., Bodin, P., & Gomberg, J. (2003). Using 1-Hz GPS data to measure deformations caused by the Denali fault earthquake. *Science*, *300*(5624), 1421–1424. https://doi.org/10.1126/science.1084531

Lay, T., Ye, L., Kanamori, H., & Satake, K. (2018). Constraining the dip of shallow, shallowly dipping thrust events using long-period love wave radiation patterns: Applications to the 25 October 2010 Mentawai, Indonesia, and 4 May 2018 Hawaii Island earthquakes. *Geophysical Research Letters*, *45*(19), 10–342. https://doi.org/10.1029/2018GL080042

Liu, C., Lay, T., & Xiong, X. (2018). Rupture in the 4 May 2018 M_w6.9 earthquake seaward of the Kilauea east rift zone fissure eruption in Hawaii. *Geophysical Research Letters*, *45*(18), 9508–9515. https://doi.org/10.1029/2018GL079349

Madariaga, R., Ruiz, S., Rivera, E., Leyton, F., & Baez, J. C. (2019). Near-field spectra of large earthquakes. *Pure and Applied Geophysics*, *176*(3), 983–1001. https://doi.org/10.1007/s00024-018-1983-x

Mattioli, G. S., Phillips, D. A., Hodgkinson, K. M., Walls, C., Mencin, D. J., Bartel, B. A., et al. (2020). The GAGE data and field response to the 2019 Ridgecrest earthquake sequence. *Seismological Research Letters*, *91*(4), 2075–2086. https://doi.org/10.1785/0220190283

Melbourne, T. I., Szeliga, W. M., Santillan, V. M., & Scrivner, C. W. (2021). Global navigational satellite system seismic monitoring. *Bulletin of the Seismological Society of America*, *111*(3), 1248–1262. https://doi.org/10.1785/0120200356

Melgar, D., Allen, R. M., Riquelme, S., Geng, J., Bravo, F., Baez, J. C., et al. (2016). Local tsunami warnings: Perspectives from recent large events. *Geophysical Research Letters*, *43*(3), 1109–1117. https://doi.org/10.1002/2015GL067100

Melgar, D., & Bock, Y. (2015). Kinematic earthquake source inversion and tsunami runup prediction with regional geophysical data. *Journal of Geophysical Research: Solid Earth*, *120*(5), 3324–3349. https://doi.org/10.1002/2014JB011832

Melgar, D., Bock, Y., & Crowell, B. W. (2012). Real-time centroid moment tensor determination for large earthquakes from local and regional displacement records. *Geophysical Journal International*, *188*(2), 703–718. https://doi.org/10.1111/j.1365-246x.2011.05297.x

Melgar, D., Bock, Y., Sanchez, D., & Crowell, B. W. (2013). On robust and reliable automated baseline corrections for strong motion seismology. *Journal of Geophysical Research: Solid Earth*, *118*(3), 1177–1187. https://doi.org/10.1002/jgrb.50135

Melgar, D., Crowell, B. W., Bock, Y., & Haase, J. S. (2013). Rapid modeling of the 2011 M_w 9.0 Tohoku-Oki earthquake with seismogeodesy. *Geophysical Research Letters*, *40*(12), 2963–2968. https://doi.org/10.1002/grl.50590

Melgar, D., Crowell, B. W., Geng, J., Allen, R. M., Bock, Y., Riquelme, S., et al. (2015). Earthquake magnitude calculation without saturation from the scaling of peak ground displacement. *Geophysical Research Letters*, *42*(13), 5197–5205. https://doi.org/10.1002/2015GL064278

Minson, S. E., Murray, J. R., Langbein, J. O., & Gomberg, J. S. (2014). Real-time inversions for finite fault slip models and rupture geometry based on high-rate GPS data. *Journal of Geophysical Research: Solid Earth*, *119*(4), 3201–3231. https://doi.org/10.1002/2013JB010622

Miyazaki, S. I., Larson, K. M., Choi, K., Hikima, K., Koketsu, K., Bodin, P., et al. (2004). Modeling the rupture process of the 2003 September 25 Tokachi-Oki (Hokkaido) earthquake using 1-Hz GPS data. *Geophysical Research Letters*, *31*(21), L21603. https://doi.org/10.1029/2004gl021457

Murray, J. R., Bartlow, N., Bock, Y., Brooks, B. A., Foster, J., Freymueller, J., et al. (2020). Regional global navigation satellite system networks for crustal deformation monitoring. *Seismological Research Letters*, *91*(2A), 552–572. https://doi.org/10.1785/0220190113

Nikolaidis, R., Bock, Y., Jonge, P., Shearer, P., Agnew, D., & Van Domselaar, M. (2001). Seismic wave observations with the global positioning system. *Journal of Geophysical Research*, *106*(B10), 21897–21916. https://doi.org/10.1029/2001JB000329

Ohta, Y., Kobayashi, T., Tsushima, H., Miura, S., Hino, R., Takasu, T., et al. (2012). Quasi real-time fault model estimation for near-field tsunami forecasting based on RTK-GPS analysis: Application to the 2011 Tohoku-Oki earthquake (M_w 9.0). *Journal of Geophysical Research*, *117*(B2), B02311. https://doi.org/10.1029/2011jb008750

Okal, E. A., Fritz, H. M., Synolakis, C. E., Borrero, J. C., Weiss, R., Lynett, P. J., et al. (2010). Field survey of the Samoa tsunami of 29 September 2009. *Seismological Research Letters*, *81*(4), 577–591. https://doi.org/10.1785/gssrl.81.4.577

O'Toole, T. B., Valentine, A. P., & Woodhouse, J. H. (2013). Earthquake source parameters from GPS-measured static displacements with potential for real-time application. *Geophysical Research Letters*, *40*(1), 60–65. https://doi.org/10.1029/2012gl054209

Polet, J., & Kanamori, H. (2000). Shallow subduction zone earthquakes and their tsunamigenic potential. *Geophysical Journal International*, *142*(3), 684–702. https://doi.org/10.1046/j.1365-246x.2000.00205.x

Riquelme, S., Bravo, F., Melgar, D., Benavente, R., Geng, J., Barrientos, S., & Campos, J. (2016). W phase source inversion using high-rate regional GPS data for large earthquakes. *Geophysical Research Letters*, *43*(7), 3178–3185. https://doi.org/10.1002/2016GL068302

Riquelme, S., Medina, M., Bravo, F., Barrientos, S., Campos, J., & Cisternas, A. (2018). W-phase real-time implementation and network expansion from 2012 to 2017: The experience in Chile. *Seismological Research Letters*, *89*(6), 2237–2248. https://doi.org/10.1785/0220180146

Rivera, L., & Kanamori, H. (2009). Using W phase for regional tsunami warning and rapid earthquake hazard assessment. In *The 2nd international workshop on earthquake early warning*. Kyoto.

Ruhl, C. J., Melgar, D., Geng, J., Goldberg, D. E., Crowell, B. W., Allen, R. M., et al. (2019). A global database of strong-motion displacement GNSS recordings and an example application to PGD scaling. *Seismological Research Letters*, *90*(1), 271–279. https://doi.org/10.1785/0220180177

Sagiya, T. (2004). A decade of GEONET: 1994-2003 the continuous GPS observation in Japan and its impact on earthquake studies. *Earth Planets and Space*, *56*(8), xxix–xli. https://doi.org/10.1186/bf03353077

Sagiya, T., Miyazaki, S. I., & Tada, T. (2000). Continuous GPS array and present-day crustal formation of Japan. *Pure and Applied Geophysics*, *157*(11–12), 2303–2322. https://doi.org/10.1007/978-3-0348-7695-7_26

Sato, M., Fujita, M., Matsumoto, Y., Ishikawa, T., Saito, H., Mochizuki, M., & Asada, A. (2013). Interplate coupling off northeastern Japan before the 2011 Tohoku-Oki earthquake, inferred from seafloor geodetic data. *Journal of Geophysical Research: Solid Earth*, *118*(7), 3860–3869. https://doi.org/10.1002/jgrb.50275

Satriano, C., Kiraly, E., Bernard, P., & Vilotte, J.-P. (2012). The 2012 M_w 8.6 Sumatra earthquake: Evidence of westward sequential seismic ruptures associated to the reactivation of a N-S Ocean fabric. *Geophysical Research Letters*, *39*(15), L15302. https://doi.org/10.1029/2012GL052387

Saunders, J. K., Goldberg, D. E., Haase, J. S., Bock, Y., Offield, D. G., Melgar, D., et al. (2016). Seismogeodesy using GPS and low-cost MEMS accelerometers: Perspectives for earthquake early warning and rapid response. *Bulletin of the Seismological Society of America*, *106*(6), 2469–2489. https://doi.org/10.1785/0120160062

Scott, E. (2021). Strike-slip tsunamis. *Nature Reviews Earth & Environmen*t, 2(6), 379. https://doi.org/10.1038/s43017-021-00179-3

Smyth, A., & Wu, M. (2007). Multi-rate Kalman filtering for the data fusion of displacement and acceleration response measurements in dynamic system monitoring. *Mechanical Systems and Signal Processing*, *21*(2), 706–723. https://doi.org/10.1016/j.ymssp.2006.03.005

Tanioka, Y., Ruff, L., & Satake, K. (1997). What controls the lateral variation of large earthquake occurrence along the Japan Trench? *Island Arc*, *6*(3), 261–266. https://doi.org/10.1111/j.1440-1738.1997.tb00176.x

Tozer, B., Sandwell, D. T., Smith, W. H., Olson, C., Beale, J. R., & Wessel, P. (2019). Global bathymetry and topography at 15 arc sec: SRTM15+. *Earth and Space Science*, *6*(10), 1847–1864. https://doi.org/10.1029/2019ea000658

Tsuboi, S., Abe, K., Takano, K., & Yamanaka, Y. (1995). Rapid determination of M_w from broadband *P* waveforms. *Bulletin of the Seismological Society of America*, *85*(2), 606–613. https://doi.org/10.1785/BSSA0850020606

Tsuboi, S., Whitmore, P. M., & Sokolowski, T. J. (1999). Application of M_{wp} to deep and teleseismic earthquakes. *Bulletin of the Seismological Society of America*, *89*(5), 1345–1351. https://doi.org/10.1785/BSSA0890051345

Wang, D., Becker, N. C., Walsh, D., Fryer, G. J., Weinstein, S. A., McCreery, C. S., et al. (2012). Real-time forecasting of the April 11, 2012 Sumatra tsunami. *Geophysical Research Letters*, *39*(19), L19601. https://doi.org/10.1029/2012GL053081

Wessel, P., Smith, W. H., Scharroo, R., Luis, J., & Wobbe, F. (2013). Generic mapping tools: Improved version released. *Eos, Transactions American Geophysical Union*, *94*(45), 409–410. https://doi.org/10.1002/2013EO450001

Whitmore, P. M., Tsuboi, S., Hirshorn, B., & Sokolowski, T. J. (2002). Magnitude-dependent correction for M_{wp}. *Science of Tsunami Hazards. The International Journal of The Tsunami Society*, *20*(4).

Withers, M., Aster, R., Young, C., Beiriger, J., Harris, M., Moore, S., & Trujillo, J. (1998). A comparison of select trigger algorithms for automated global seismic phase and event detection. *Bulletin of the Seismological Society of America*, *88*(1), 95–106. https://doi.org/10.1785/BSSA0880010095

Wright, T. J., Houlié, N., Hildyard, M., & Iwabuchi, T. (2012). Real-time, reliable magnitudes for large earthquakes from 1 Hz GPS precise point positioning: The 2011 Tohoku-Oki (Japan) earthquake. *Geophysical Research Letters*, *39*(12), L12302. https://doi.org/10.1029/2012gl051894

Ye, L., Lay, T., Kanamori, H., & Rivera, L. (2016). Rupture characteristics of major and great ($M_w \geq 7.0$) megathrust earthquakes from 1990 to 2015: 1. Source parameter scaling relationships. *Journal of Geophysical Research: Solid Earth*, *121*(2), 826–844. https://doi.org/10.1002/2015JB012426

Yokota, Y., Ishikawa, T., & Watanabe, S. I. (2018). Seafloor crustal deformation data along the subduction zones around Japan obtained by GNSS-A observations. *Scientific Data*, *5*(1), 1–11. https://doi.org/10.1038/sdata.2018.182

Erratum

In the originally published version of this article, equation 1 contained a typographical error. The error involved the omission of an alpha in the denominator of the last term (under AFS). The error has been corrected, and this may be considered the authoritative version of the record.